The Astrophysical Journal, 995:7 (11pp), 2025 December 10 https://doi.org/10.3847/1538-4357/ae1477

Determining the State of Jupiter's Magnetosphere Using In Situ and Remote Sensing Observations

J. W. Sun[1,2], L. Xie[1,2], Z. H. Yao[3], S. Y. Fu[1], B. Zhang[3], Y. Xu[4], F. Leppard[3], Y. N. Chen[4], D. Grodent[5], L. C. Ray[6], B. Bonfond[5], and W. R. Dunn[7]
[1] School of Earth and Space Sciences, Peking University, Beijing, People's Republic of China; xielun@pku.edu.cn
[2] State Key Laboratory of Solar Activity and Space Weather, National Space Science Center, Chinese Academy of Sciences, Beijing 100190, People's Republic of China
[3] Department of Earth & Planetary Sciences, University of Hong Kong, Hong Kong, People's Republic of China; yaozh@hku.hk
[4] Department of Earth and Space Sciences, Southern University of Science and Technology, Shenzhen, People's Republic of China
[5] Laboratoire de Physique Atmosphérique et Planétaire, STAR Institute, Université de Liège, Liège, Belgium
[6] Department of Physics, Lancaster University, Lancaster, UK
[7] Department of Physics and Astronomy, University College London, London, UK
Received 2025 August 4; revised 2025 October 12; accepted 2025 October 14; published 2025 December 2

Abstract

While Jupiter's magnetosphere is primarily governed by internal processes, variations in solar wind conditions can significantly modulate magnetospheric energy. Assessing solar wind conditions at Jupiter has been a long-standing challenge in the community. In this study, we investigate multiple datasets, including auroral images captured by the Hubble Space Telescope and in situ measurements obtained by the Juno spacecraft, to characterize Jupiter's magnetosphere during solar wind compression and quiet conditions. The distinct responses demonstrate that auroral morphologies, lobe magnetic fields, ultra-low-frequency waves, and broadband kilometric radio emissions could serve as effective indicators for magnetospheric states. In particular, we statistically analyze the distribution of lobe magnetic fields, which represent the intensities of the cross-field electrical currents in the magnetodisc, and propose the applicability of the lobe magnetic field as a proxy for solar wind conditions. The results from the four individual methods of determining magnetospheric states are generally consistent, providing further evidence of their robustness. These observational proxies for solar wind conditions could therefore be widely applied in both existing spacecraft datasets and those from future missions to Jupiter.

Unified Astronomy Thesaurus concepts: Jupiter (873); Planetary magnetospheres (997); Solar-planetary interactions (1472)

1. Introduction

Planetary magnetospheres are continuously immersed in the solar wind, which influences their global morphology and drives dynamics through energy transfer (C. T. Russell 2001). Distinguishing and monitoring magnetospheric states, whether strongly compressed by the solar wind or expanded under quiet conditions, is crucial for advancing our understanding of dynamic magnetospheric processes beyond static equilibrium descriptions. Among the planets in the solar system, Jupiter has the strongest magnetic field and the largest magnetosphere (e.g., F. Bagenal 2007), making it a unique laboratory for investigating solar wind–magnetosphere interactions at extreme scales and yielding insights into fundamental magnetospheric physics.

However, unlike Earth, with spacecraft positioned at the L1 point that can continuously monitor in situ solar wind parameters, Jupiter and other planets lack such upstream measurements for real-time determination of magnetospheric states. Solar wind conditions at outer planets are typically estimated by extrapolating Earth-based measurements using propagation models (D. Odstrcil 2003; C. Tao et al. 2005; B. Zieger & K. C. Hansen 2008; M. Owens et al. 2020; L. Barnard & M. Owens 2022; T. B. Keebler et al. 2022; M. J. Rutala et al. 2024). While these models provide valuable quantitative estimates, they are nevertheless constrained by the complexity of solar wind evolution. For Jupiter specifically, model validations against in situ measurements have revealed timing uncertainties reaching ± 4 days (C. Tao et al. 2005; B. Zieger & K. C. Hansen 2008; L. K. Jian et al. 2015; T. B. Keebler et al. 2022; M. A. Reiss et al. 2023; M. J. Rutala et al. 2024). This level of uncertainty is a crucial limit to our understanding of Jupiter's magnetospheric dynamics that often exhibit significant changes on smaller timescales (D. A. Gurnett et al. 2002; N. Krupp et al. 2004; J. D. Nichols et al. 2017), hindering temporal correlation studies and the identification of response mechanisms.

Potentially, these challenges could be partially addressed through in situ observations. Spacecraft at Jupiter can capture solar wind parameters outside the magnetosphere (e.g., R. W. Ebert et al. 2014; D. J. McComas et al. 2017) or acquire magnetopause standoff distances during boundary crossings (e.g., E. J. Smith et al. 1978; H. S. Bridge et al. 1979a, 1979b; S. J. Bame et al. 1992). However, such direct measurements also have limitations: acquiring upstream conditions typically sacrifices contemporaneous magnetospheric monitoring, and spacecraft spend the majority of their operational time inside the magnetosphere, where direct measurement of solar wind parameters is not feasible.

To enable continuous magnetospheric state examination, robust correlations between external solar wind conditions and internal magnetospheric responses would be highly valuable. Once validated, these correlations allow us to identify magnetospheric states using continuously observable proxies, facilitating further studies on solar wind–magnetosphere interactions even without direct upstream measurements and temporally accurate model output. Establishing these correlations critically depends on coordinated observations to separate spatial and temporal effects. Key opportunities include: (1) Multispacecraft conjunctions (e.g., the Cassini–Galileo overlap period; N. Krupp et al. 2002; W. S. Kurth et al. 2002) enabling simultaneous solar wind and magnetospheric measurements, and (2) synergistic use of remote sensing data (e.g., auroral emissions monitored by telescopes and spacecraft) alongside in situ measurements of solar wind (e.g., J. D. Nichols et al. 2007, 2017) or magnetospheric phenomena (e.g., Z. H. Yao et al. 2022). These joint datasets have been leveraged in previous studies to establish linkages between upstream solar wind conditions and various magnetospheric responses, including auroras, magnetic fields, ultra-low-frequency (ULF) waves, and radio emissions (as will be detailed in Section 2).

In this study, we consolidate these diverse observational signatures to reveal that Jupiter's magnetosphere exhibits two distinct states ("compressed" and "quiet") under varying solar wind forcing. We further develop and present practical identification criteria using available in situ and remote sensing measurements, and verify their effectiveness via cross-validation using Juno's measurements.

2. Potential Proxies for Jovian Magnetospheric States

In this section, we evaluate four-potential proxies for Jovian magnetospheric states, reviewing their documented responses to varying external conditions. We develop an identification framework for each proxy, based on its observational characteristics and distributions, detailing specific criteria, valid ranges of applicability, and practical considerations. The analysis primarily utilizes data from the Juno spacecraft, which carries the MAG instrument for magnetic field measurements (J. E. P. Connerney et al. 2017) and the Waves instrument for observing radio emissions (W. S. Kurth et al. 2017). Applying the classification methods to a comprehensive dataset spanning from 2016 July 7 to 2023 July 7, we generate time catalogs of both quiet and compressed states for further analysis.

2.1. Auroras

Auroral emissions serve as a direct proxy of energy dissipation in the magnetosphere (Z. H. Yao et al. 2019; B. Bonfond et al. 2021). Coordinated datasets of in situ measurements and remote auroral imaging provide an unprecedented opportunity to connect auroral morphologies to upstream drivers. D. A. Gurnett et al. (2002) presented a seminal case with simultaneous observations, in which Cassini and Galileo sequentially captured interplanetary shock signals near Jupiter, followed by a peak in auroral intensities detected by Cassini's UV spectrograph. Similarly, J. D. Nichols et al. (2007, 2017) combined in situ interplanetary measurements with Hubble Space Telescope (HST) auroral observations, revealing that the brightness of Jupiter's main emissions significantly increased during enhanced solar wind conditions compared to quiet intervals. Furthermore, Z. H. Yao et al. (2022) conducted a comprehensive statistical analysis, demonstrating that all compression events associated with reduced magnetopause standoff distances coincided with main auroral brightening (MAB) morphologies, with no instances of dim auroral emissions. Subsequent studies by L. A. Head et al. (2024, 2025) further elucidated that magnetospheric compression could trigger a global contraction of the main emissions, along with the appearance of auroral bridges. These results collectively confirm that Jupiter's auroral morphology, particularly the main emissions, indeed exhibits significant modulation under different solar wind conditions.

The classification framework proposed by D. Grodent et al. (2018) discriminates between different auroral morphologies and categorizes them into six families. Among them, the X-family auroras (consistent with the definition of MAB events; see Figure 1(a)) display a bright, narrow, and sharply defined band on the dawnside, often accompanied by dynamic structures in the dusk sector. In contrast, the Q-family auroras (Figure 1(b)) exhibit extremely low emission power, with the main emissions often barely distinguishable. Based on the studies discussed above, the Q-family auroras are believed to correspond to a quiet and undisturbed magnetosphere, while the X-family auroras indicate significant magnetospheric compression. D. Grodent et al. (2018) and B. Palmaerts et al. (2024) systematically labeled auroral images obtained from the HST programs GO-14634 and GO-15638, respectively. From their lists, we obtain a total of 19 quiet (Q-family) and 14 compressed (X-family) magnetospheric events. While morphological classification involves inherent subjectivity, this aurora-derived dataset provides a valuable benchmark: unlike single-point measurements, auroral imaging captures the global magnetospheric state instantaneously. And its reliability is anchored in correlations directly established through unambiguous, simultaneous observations of auroral morphologies and solar wind conditions.

2.2. Statistical Distribution of Lobelike Magnetic Fields

Due to the tilt between Jupiter's magnetic dipole and its rotation axis, the current sheet oscillates with a period of approximately 10 hr. Consequently, spacecraft periodically enter the current sheet and exit into regions characterized by relatively stable magnetic field strengths and low plasma density, as shown in Figures 2(a) and (b). While sharing similarities with the terrestrial magnetospheric lobes, these regions are not identical with the distant lobe; we therefore designate them as lobelike regions. Z. H. Yao et al. (2019) extracted lobelike magnetic field ($B_{\mathrm{lobe-like}}$) values and demonstrated a clear correlation between $B_{\mathrm{lobe-like}}$ variations and auroral morphology. Y. Xu et al. (2023) further demonstrated that under quiet conditions, $B_{\mathrm{lobe-like}}$ values across different radial distances follow a fitting curve (the gray line in Figures 1(c) and (d)) that is distinct from that observed during compressed times (blue line in Figure 1(c)). The two curves reflect variations in the lobelike magnetic field strengths and a global enhancement of magnetodisk current intensities under solar wind compression compared to the quiet period. These observed differences and variations suggest that $B_{\mathrm{lobe-like}}$ can serve as a reliable indicator of magnetospheric state. Furthermore, the lobelike regions just outside the current sheet at low latitudes are particularly well suited to capture the signature while minimizing confounding contributions from other current systems and the latitudinal variation of the planetary dipole field.

Specifically, we identified 10 hr intervals (approximately one Jovian rotation period) containing current sheet crossings.

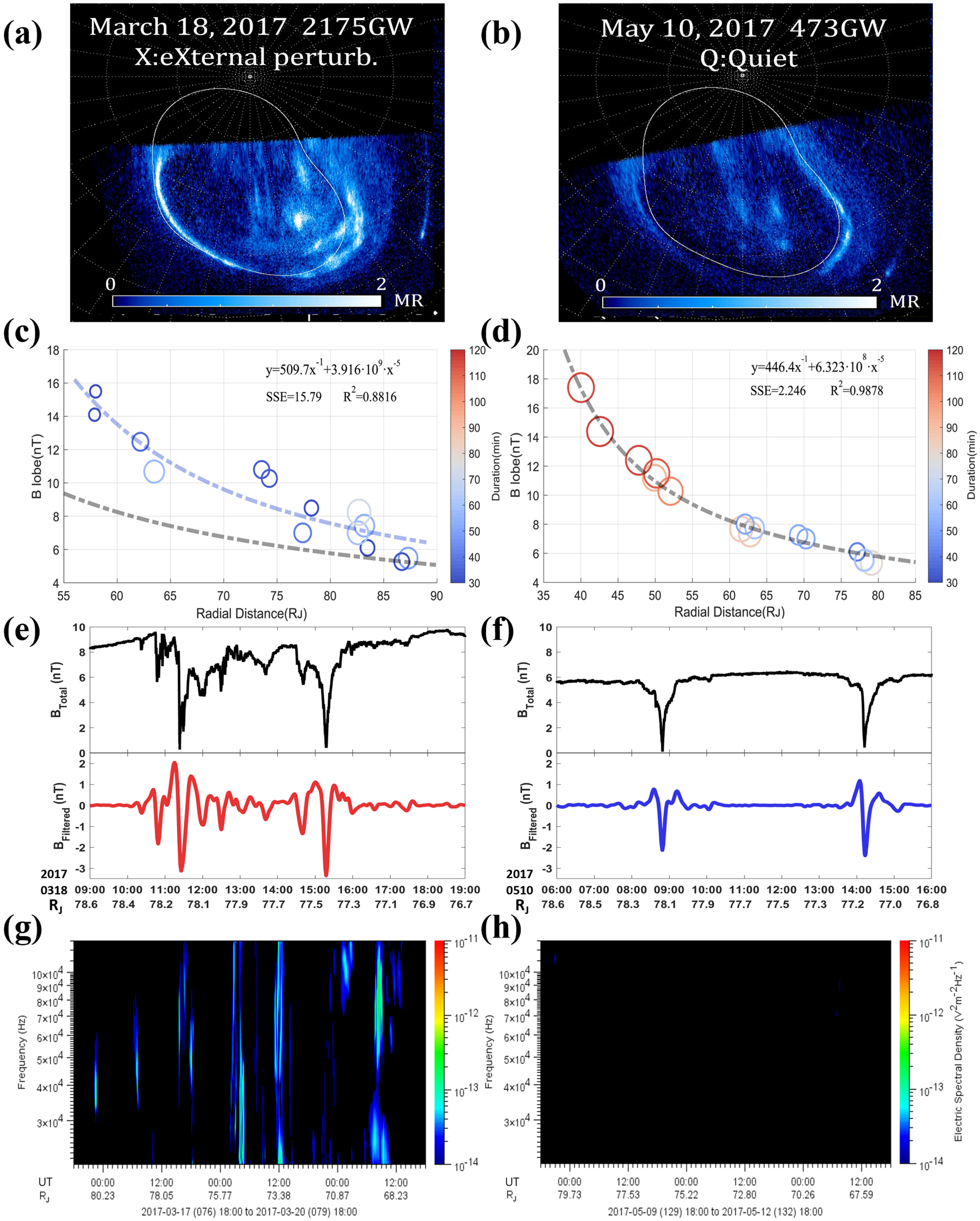

Figure 1. Comparisons of magnetospheric phenomena between compressed and quiet states. Two representative UV auroral images for the (a) X-family aurora and (b) Q-family aurora identified by D. Grodent et al. (2018). Each image is labeled with the observation date, total power, and auroral morphology. The magnetic field in the lobelike region, $B_{\mathrm{lobe-like}}$, across different radial distances in (c) the compressed (blue) and (d) the quiet (gray) magnetosphere (from Y. Xu et al. 2023). Each circle's color and size in (c), (d) represent the duration of the spacecraft crossing the current sheet, a proxy for the current sheet thickness. Total magnetic field strengths and magnetic field fluctuations using a fourth-order Butterworth filter to produce 10–60 minutes bandpass-filtered results of (e) the compressed magnetosphere, which shows significant fluctuations, and (f) the quiet magnetosphere, where almost no magnetic field fluctuations appear (modified from J. W. Sun et al. 2024). Measurements of radio emissions in (g) the compressed magnetosphere, showing prominent broadband kilometric (bKOM) emission features and (h) quiet magnetosphere where almost no bKOM radio emissions are detected (modified from Y. Chen et al. 2024). These phenomena present concurrent responses to changes in the magnetospheric states.

Within each interval, the lobelike region was automatically selected by requiring the variance of magnetic field strengths within a sliding window to fall below the 10th percentile threshold computed across the entire interval. As shown in Figure 2(c), these selected regions consistently exhibit the expected characteristics: quasi-constant magnetic field and low plasma density. We then computed the average magnetic field strength over these selected lobelike subintervals during each

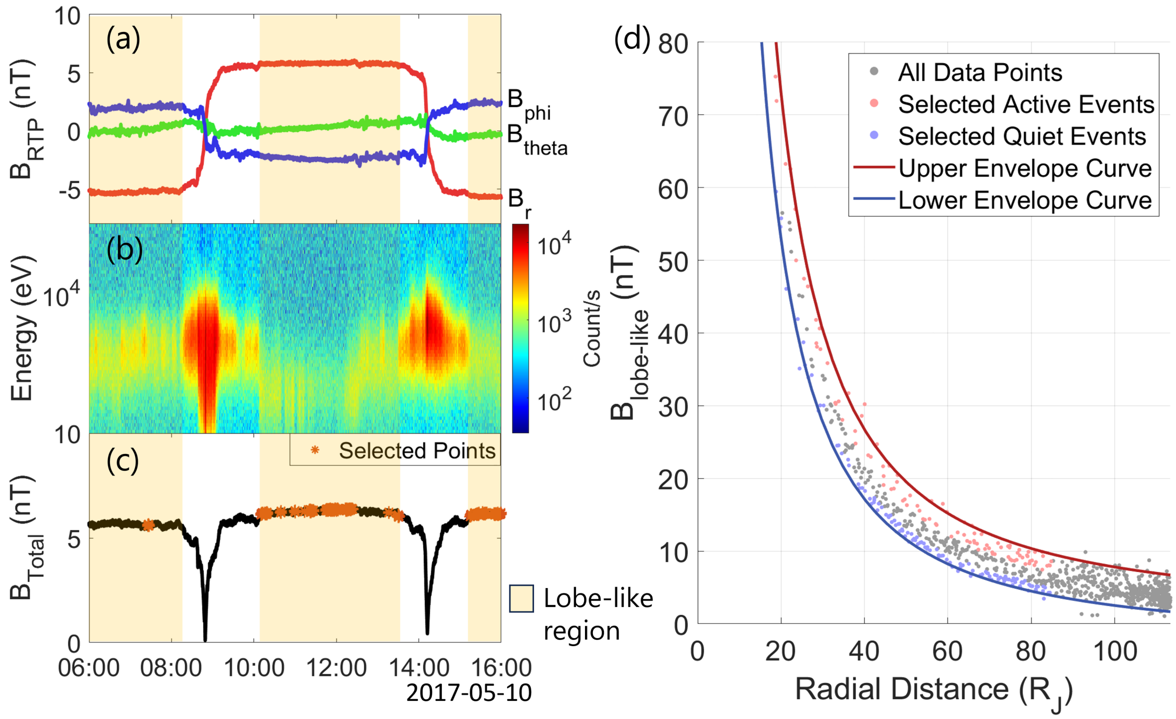

Figure 2. Identification of magnetospheric states based on $B_{\mathrm{lobe-like}}$ measurements. (a-c) illustrate the lobelike region selection process with data from 2017 May 10. (a) R-Theta-Phi magnetic field components in Jupiter-De-Spun-Sun (JSS) coordinates. (b) 100 eV–100 keV electron energy spectra measured by Jovian Auroral Distributions Experiment (JADE). (c) Total magnetic field strength. Orange stars denote points algorithmically selected as lobelike using the criterion described in the main text. The orange shading indicates regions manually identified as lobelike based on a quasi-constant magnetic field and low plasma density. These points all lie within the orange-shaded regions, which demonstrates the reliability and effectiveness of our lobelike region selection method. (d) Radial distribution of measured $B_{\mathrm{lobe-like}}$. Red and blue curves indicate fitted upper and lower envelopes, respectively. Events are classified as compressed (light red; higher $B_{\mathrm{lobe-like}}$) or quiet (light blue; lower $B_{\mathrm{lobe-like}}$) based on these envelopes.

Jovian rotation period to obtain the measured $B_{\mathrm{lobe-like}}$. The distribution of $B_{\mathrm{lobe-like}}$ in Figure 2(d) exhibits a finite thickness. This spread reflects variations of $B_{\mathrm{lobe-like}}$ influenced by the intensity of the nearby disk currents. We compared the calculated $B_{\mathrm{lobe-like}}$ values during the mission with the expected $B_{\mathrm{lobe-like}}$ values typical of a compressed or quiet magnetosphere to classify the magnetospheric states. As displayed in Appendix A, the two curves in Y. Xu et al. (2023) can effectively classify events at 55–80 R_J into distinct categories: events with $B_{\mathrm{lobe-like}}$ values near or above the upper curve are considered compressed events, while those near or below the lower curve are quiet events. At other locations, however, most events cluster within the same population and cannot be separated by the two curves, which is reasonable given that the model and dataset used in Y. Xu et al. (2023) primarily focus on 55–80 R_J and lack constraints at other regions.

To better characterize $B_{\mathrm{lobe-like}}$ across different magnetospheric states and extend the method's applicability, we delineated the envelopes of $B_{\mathrm{lobe-like}}$'s radial distribution. For the functional form of the envelopes, we adopt the expression: $B_{\mathrm{lobe-like}} = \sqrt{\vec{B}^2_{\mathrm{dipole}} + \vec{B}^2_{\mathrm{sheet}}} = \sqrt{\frac{a}{r^6} + \frac{b}{r^n}} + c$, where $\frac{a}{r^6}$ originates from the characteristic r^{-3} decay of the planetary dipole field, while $\frac{b}{r^n}$ represents contributions from current-induced magnetic fields. The exponent n depends on the radial dependence of disk currents, and the coefficient b scales with the current intensity. Through fitting procedures (detailed in Appendix A), we obtain upper and lower envelope curves with the following analytical expressions:

$$\text{Upper Curve:} \quad B_{\mathrm{lobe-like}} = \sqrt{\frac{1.167 \times 10^8}{r^6} + \frac{4.102 \times 10^7}{r^3}} + 1.408 \tag{1}$$

$$\text{Lower Curve:} \quad B_{\mathrm{lobe-like}} = \sqrt{\frac{1.108 \times 10^8}{r^6} + \frac{2.454 \times 10^7}{r^3}} - 2.432. \tag{2}$$

The expressions for both upper and lower envelopes have similar a values, in agreement with our theoretical expectation that the first term primarily originates from the invariant intrinsic magnetic field contribution. The identical exponent $n = 3$ indicates consistent radial dependence of disk currents under different magnetospheric states. The differing b values quantitatively demonstrate stronger current intensities during compressed periods compared to quiet intervals, matching the results reported in Y. Xu et al. (2023). Collectively, these comparisons support the overall reasonability of the fitting results.

The envelope curves enable systematic determination of magnetospheric states across extended radial distances as displayed in Figure 2(d). We classify the magnetosphere as quiet when $B_{\mathrm{lobe-like}} < B_{\mathrm{lower}} + 0.2 \times B_{\mathrm{minus}}$, where B_{lower} is the value given by the lower envelope curve and B_{minus} denotes the difference between the two curves; conversely, it is classified as a compressed state when $B_{\mathrm{lobe-like}} > B_{\mathrm{upper}} - 0.45 \times B_{\mathrm{minus}}$, where B_{upper} is given by the upper envelope curve and the different coefficients are chosen because the data points near the upper envelope exhibit a sparser distribution compared to those near the lower envelope. We apply this criterion within 15–85 R_J. For regions inside 15 R_J, the magnetic field is dominated by Jupiter's intrinsic field, with current-induced variations contributing little. Beyond 85 R_J, the $B_{\mathrm{lobe-like}}$ values under the two states gradually converge as shown in Figures 1(c) and (d), making them nearly indistinguishable and introducing uncertainties. Through the criterion, we identify 118 quiet magnetospheric intervals and 99 compressed magnetospheric intervals (each event interval spans 10 hr, with a total of 414 qualified windows). The light red and blue points in Figure 2(d) mark our selected events, respectively.

2.3. ULF Waves

ULF waves play a crucial role in energy transfer within the magnetosphere. Both theoretical models and studies on Earth have shown that ULF wave activity is closely associated with variations in interplanetary conditions and auroral emissions (Q. Zong et al. 2017). In Jupiter's magnetosphere, D. Pan et al. (2021) demonstrated that ULF wave intensities correlate significantly with the main aurora emissions and possibly also with polar emissions. Furthermore, J. W. Sun et al. (2024) established a correlation between quiet magnetospheric conditions and a low occurrence rate of 10–60 minutes ULF wave events, while these signals were observed across all time durations under compressed states identified according to auroral morphology. Figures 1(e) and (f) show the magnetic field fluctuations during compressed and quiet magnetospheric intervals, respectively. These results demonstrate that ULF wave activity in Jupiter's magnetosphere distinctly differs between compressed and quiet states under strong and weak solar wind conditions, suggesting ULF waves may serve as an effective proxy for determining magnetospheric states.

State identification based on temporal variations of magnetospheric phenomena requires careful discrimination against artifacts introduced by the parameter's intrinsic spatial distribution and the spacecraft's changing position within the magnetosphere. J. W. Sun et al. (2024) identified significant latitudinal differences in ULF wave occurrence rates within Jupiter's magnetosphere, necessitating region-specific threshold adjustments. Here, our analysis primarily focuses on measurements in low-latitude regions exhibiting current sheet crossings within 10 hr windows for state classification, as these regions provide better ULF wave detectability. We performed wavelet analysis on 1 s resolution magnetic field data and integrated the power spectral density across the 10–60 minutes period range over 10 hr windows. ULF wave energies in Jupiter's magnetosphere statistically vary with radial distance (H. Manners & A. Masters 2020). Accordingly, we binned the data by radial distance and identified events with wave intensities in the highest 25th percentile within each bin as compressed intervals, while those in the lowest 25th percentile were classified as quiet intervals. The same analytical processes were applied to both the total magnetic fields and the three background-subtracted magnetic field components in the mean field-aligned (MFA) coordinate system, enabling us to examine the responses of compressional, transverse, and overall wave activities. As shown in Appendix B, cross-validation revealed that fluctuations in all components potentially distinguish between magnetospheric states, with compressional waves demonstrating the best performance. This superiority likely stems from compressional waves' role as a more immediate conduit for solar wind energy input: external solar wind variations perturb the magnetopause, first launching fast-mode compressional waves that penetrate and undergo transformation within the magnetosphere (S. N. Bentley et al. 2018). The correlation between compressional mode waves and X-ray flares reported in Z. Yao et al. (2021) also suggests the crucial role of compressional waves in magnetospheric energy transport. Therefore, we selected compressional wave intensities as the diagnostic criterion, determining 213 intervals of quiet magnetospheric conditions and 213 intervals of compressed conditions (each event interval spans 10 hr, with a total of 881 qualified windows).

2.4. Radio Emissions

Radio emissions offer a direct probe into particle acceleration sites and show potential as indicators of magnetospheric dynamics (e.g., B. Cecconi et al. 2022; A. R. Fogg et al. 2022). Jupiter's magnetosphere exhibits extensive radio emissions, among which broadband kilometric (bKOM) emissions are believed to be particularly sensitive to solar wind conditions (P. Zarka et al. 2021). Case studies by C. K. Louis et al. (2023) revealed that magnetospheric compressions could activate new radio sources, especially bKOM emissions. Y. Chen et al. (2024) performed statistical analyses and demonstrated that during compressed states (identified based on magnetopause standoff distances measured during boundary crossings), Jovian bKOM emissions exhibited approximately 10 hr periodic occurrences with extended durations and broader frequency ranges. Conversely, in an expanded magnetosphere, bKOM emissions are typically absent, and the occasionally observed emissions are also characterized by shorter durations and narrower frequency ranges. Figures 1(g) and (h) illustrate this comparison under compressed and quiet conditions, respectively.

To characterize the duration and frequency range of bKOM burst events comprehensively, we employed an area-based metric. This metric is defined as the total number of spectrogram grid points where the spectral density exceeded a predefined threshold (A) within the ∼20–140 kHz frequency band (the LFR_HI channels) in a 10 hr time window. In addition to metrics evaluated over one rotation period, persistent patterns, such as periodic enhancements or prolonged time durations of quiescence, could also provide critical constraints for identifying states of magnetospheric disturbance or stability. Our criteria specify that intervals are classified as quiet if the area remains below the quiet-state threshold (B) for more than seven consecutive rotation periods, and as compressed if the area exceeds an active-state threshold (C) for more than three consecutive rotation periods. This persistence-based criterion helps reduce false positives associated with transient bursts or localized fluctuations. Considering the latitudinal dependence of bKOM emission occurrence rates reported by C. K. Louis et al. (2021), region-specific adjustments to the classification thresholds are necessary when analyzing measurements at different latitudes. The thresholds adopted in this study for Juno's low-latitude measurements with current sheet crossings during 10 hr windows were set as $A = 5 \times 10^{-14}$ $\mathrm{V^2\,m^{-2}\,Hz^{-1}}$ for spectral density, $B = 500$ grid points for the quiet state, and $C = 3000$ grid points for the compressed state. We identified 237 quiet and 219 compressed intervals (each interval spans 10 hr, with a total of 885 qualified windows).

Table 1
Determination of Magnetospheric States during Q-family Aurora Intervals Using Single-point Measurement Methods

Index	Q-family Aurora Event Time (UT)	$B_{\mathrm{lobe-like}}$	ULF Waves	BKOM Radio Emissions
1	2016 Dec 4 12:44:51	×	✓	×
2	2016 Dec 12 14:40:35	/	/	/
3	2016 Dec 12 16:15:22	/	/	/
4	2016 Dec 13 11:21:37	/	/	/
5	2016 Dec 15 07:50:44	/	/	/
6	2017 May 10 05:54:33	✓	✓	✓
7	2017 May 10 10:40:39	✓	✓	✓
8	2017 May 13 08:36:44	✓	✓	✓
9	2017 May 15 11:28:13	✓	✓	✓
10	2017 Jul 5 08:05:37	✓	✓	✓
11	2017 Jul 6 23:49:38	✓	✓	✓
12	2017 Jul 8 04:28:27	✓	✓	✓
13	2017 Jul 8 06:01:24	✓	✓	✓
14	2019 Mar 9 11:10:16	/	/	/
15	2019 Mar 28 20:50:57	/	/	/
16	2019 Apr 6 14:36:00	/	/	/
17	2019 Sep 7 09:48:50	/	/	/
18	2019 Sep 10 07:42:46	×	×	×
19	2019 Sep 13 13:33:29	/	/	/

Note. The time list provides the corresponding time at Juno corrected for light travel time at the start of the HST exposure from D. Grodent et al. (2018) and B. Palmaerts et al. (2024). Symbols are defined as: ✓ indicates successful identification of the target state (consistent with auroral-morphology-based classification), × denotes failure to identify the target state, and / represents that the measurement position falls outside the method's applicable range. Here, the target state refers to the quiet state.

Table 2
Determination of Magnetospheric States during X-family Aurora Intervals Using Single-point Measurement Methods

Index	X-family Aurora Time (UT)	$B_{\mathrm{lobe-like}}$	ULF Waves	BKOM Radio Emissions
1	2016 Nov 30 14:57:23	/	✓	×
2	2016 Nov 30 16:32:45	/	✓	×
3	2016 Dec 1 16:23:32	×	✓	×
4	2016 Dec 5 18:56:58	✓	✓	✓
5	2016 Dec 6 14:02:21	✓	✓	✓
6	2016 Dec 11 18:29:20	/	/	/
7	2017 Mar 17 08:01:34	✓	✓	×
8	2017 Mar 18 14:14:38	✓	×	✓
9	2017 Mar 19 09:19:18	✓	✓	✓
10	2017 Jun 18 09:13:00	/	/	/
11	2019 May 22 21:24:30	✓	✓	✓
12	2019 May 23 16:28:33	×	×	✓
13	2019 Jul 20 13:15:38	/	/	/
14	2019 Sep 10 04:32:07	×	✓	✓

Note. The time list source and symbol definitions follow Table 1. Here, the target state refers to the compressed state.

3. Results and Cross Validation

We have summarized four methods for determining magnetospheric states: auroral morphologies, $B_{\mathrm{lobe-like}}$ values, ULF wave activities, and bKOM radio emissions. The lists of compressed and quiet intervals derived from each of these four methods are provided in J. Sun et al. (2025) in Zenodo at doi: 10.5281/zenodo.16355250. Among these potential proxies, auroral emissions offer global visibility of energy release processes, making them particularly valuable in characterizing large-scale magnetospheric responses. In this study, the aurora-derived classification dataset serves as a high-confidence benchmark against which we evaluate the reliability and applicability of the other three proxy methods. We systematically have examined whether the $B_{\mathrm{lobe-like}}$, ULF wave, and radio emission methods could correctly identify the expected quiet or compressed states during Q-family and X-family auroral events, with the results summarized in Tables 1 and 2.

The analysis shows that both the $B_{\mathrm{lobe-like}}$ and ULF wave methods generally yield consistent results with auroral morphology identification, although several misclassifications occur, possibly due to disturbances from local processes or temporal offsets between phenomena. For the results of radio emission identification, the quiet time list also shows acceptable consistency with Q-family auroral events. However, the performance in identifying compressed events is comparatively weaker. Four compression events in Table 2 were not successfully identified, three of which occurred during the early Juno orbits in 2016. Appendix C includes an illustration of Juno's orbits and the distributions of events that were correctly and incorrectly classified using the bKOM method. It can be seen that these misclassified events are mainly concentrated at large radial distances on the dawnside of Jupiter. The clustering of misidentified events may not be coincidental and likely reflects a systematic bias introduced by the orbital effects.

In addition to the clustering of misclassified events in Tables 1 and 2, the overall distributions of the classification results also provide insight into the influence of orbital effects. During Juno's prime mission phase (2016–2021), the overall shape of its orbit remained essentially unchanged, but the apoapsis gradually precessed from the dawn sector through the nightside toward the dusk sector, while the orbital inclination steadily increased. Comparing the event lists from all four methods, we found that the auroral, $B_{\rm lobe-like}$ and ULF wave approaches provided relatively balanced distributions of quiet and compressed periods across different years. In contrast, the lists identified through radio emissions exhibit systematic biases: no quiet events are recorded after 2019, and significantly fewer compressed events are identified in 2016 compared to other methods. Our analysis has already been constrained to low-latitude regions, thereby excluding effects from latitudinal dependence. As previous studies have shown that bKOM emissions display almost uniform distributions with radial distance (G. Fischer et al. 2025), the influence of radial effects can therefore be ruled out. The observed imbalance may instead arise from local time variations caused by the orbit precession. Auroras and bKOM radio emissions both originate from the precipitation of charged particles along high-latitude magnetic field lines. Given that Jupiter's auroral brightness and morphology exhibit significant local time dependence (A. Groulard et al. 2024; L. A. Head et al. 2024), it is plausible that bKOM radio emissions, which are associated with the same magnetospheric processes, may also display local time asymmetries similar to those observed in Jovian hectometric emissions and Saturn kilometric radiation (J. D. Menietti et al. 1999; L. Lamy et al. 2009; P. Zarka et al. 2021; A. Boudouma et al. 2023).

To explore potential improvements, an adjusted approach was tested: the bKOM data were normalized by local time binning, and events were then classified based on percentile rankings within each bin (events in the highest 25% were classified as compressed). The resulting list of compressed and quiet events was better balanced, comparable with other methods, and the agreement with auroral classifications was improved. This adjusted approach successfully identified most X-family auroral events, with the sole exception of Event 14. Nevertheless, we maintain a cautious stance regarding the necessity of local time corrections, which requires more comprehensive analyses of bKOM emissions' distribution.

Our comparative analysis demonstrates that $B_{\rm lobe-like}$ and ULF wave activities can effectively reproduce magnetospheric state classifications derived from auroral morphologies following appropriate spatial normalization. The bKOM radio emissions also provide an acceptable indicator with additional analysis and further correction. Collectively, these single-point measurements affirm their effectiveness as proxies of magnetospheric states. Moreover, we propose that combining multiple datasets can further enhance identification reliability by providing a more comprehensive assessment of magnetospheric states. Consistent results across different methods would significantly mitigate the interference from local processes, thereby reducing the probability of misclassification. Here, we focus on the overlapping valid application ranges of the three methods, the low-latitude region between 15 and 85 R_J, to obtain their consensus classifications. When a time window is concurrently identified as a quiet or compressed event by at least two in situ measurement methods, it is classified accordingly in the consolidated results. From a total of 414 qualified time windows, we identify 124 quiet and 113 compressed events (Sun 2025). Notably, each in situ method independently identified ∼25% of events as quiet and ∼25% as compressed, while the resulting consolidated classifications also show similar proportions (∼30% quiet, ∼27% compressed). The significant retention rates signify substantial overlap in the event sets detected by the individual techniques and demonstrate good consistency and robustness across the different methods. The consolidated time lists complement the auroral-morphology-based classifications and enable more systematic and universal investigations of solar wind–magnetosphere interactions.

4. Discussion and Summary

Jupiter's magnetosphere displays a spectrum of states in response to varying solar wind conditions. In the continuum, this study focuses on characterizing and distinguishing two archetypal states representing opposite extremes: the quiet and compressed magnetosphere. We observe enhanced auroral emissions, elevated lobe magnetic fields, increased ULF wave activities, and more active (albeit comparatively less reliable) bKOM radio emissions in the compressed magnetosphere compared to the quiet magnetosphere. These indicators allow us to determine magnetospheric states even in the absence of in situ solar wind measurements. While auroral imaging provides global visibility, using single-point in situ measurements to infer the global state of Jupiter's complex magnetosphere requires careful consideration of several factors. First, temporal averaging over full Jovian rotations (∼10 hr) is applied to comprehensively capture characteristic structures and processes across different rotational phases. Additionally, the inherent distributions of the indicators and their responses to external solar wind variations exhibit spatial variability across Jupiter's vast magnetosphere, necessitating normalization corrections or region-specific standards for accurate determination.

By addressing these considerations, our classification results derived from Juno-era data are deemed effective and reliable, as confirmed by cross-validation. Consequently, these three in situ methods enable continuous monitoring of magnetospheric states and corresponding external conditions throughout most of the spacecraft's measurement period—far exceeding the temporal coverage of remote sensing and in situ solar wind measurements. The methodology and criteria are also applicable to past missions (e.g., Galileo) and future Jupiter exploration programs, following appropriate adaptations to account for instrumental and orbital differences.

Although the use of in situ observations provides valuable diagnostics, such methods also have limitations, since the response of magnetospheric phenomena does not occur instantaneously with changes in solar wind conditions. For example, in event #18 of Table 1, none of the three in situ proxies yielded a state determination consistent with the auroral method. We noticed that approximately 3 hr before event #18, the auroral morphology still exhibited X-family features (corresponding to event #14 in Table 2), suggesting that a transition in the magnetospheric state occurred within that 3 hr interval. It is likely that Jupiter's magnetosphere underwent a brief compression, with event #14 capturing the final stage of the associated auroral response. Some 3 hr later, although the auroral signatures had faded, some other responses in the system remained in a transitional phase, retaining residual effects of the prior compression. Notably, Juno was located near 30 R_J at that time, a relatively inner region where the response to external conditions tends to exhibit a longer delay. The presence of response delays limits the ability of these observational methods to unambiguously identify the magnetospheric states. Different magnetospheric phenomena respond to external perturbations on distinct timescales, and even the same parameter may exhibit spatially dependent delays, all of which can naturally lead to occasional misclassifications. In future work, as the generation mechanisms of auroras, $B_{\mathrm{lobe-like}}$ signatures, ULF waves, and bKOM emissions become better understood, their respective response times to solar wind perturbations will be further quantified. This progress will help further refine the use of these observables as reliable proxies for solar wind conditions.

In summary, both auroral remote sensing and the three in situ methods presented here facilitate temporally precise state determinations, creating opportunities for statistical time-series analyses that can advance our understanding of planetary magnetospheric response dynamics under varying solar wind conditions. Furthermore, this framework—though developed for Jupiter—could potentially be transferred to other planetary magnetospheres (e.g., Saturn, Uranus, Neptune), pending validation with respective mission data in the future.

Acknowledgments

All Juno data used here are publicly available from NASA's Planetary Data System (https://pds-ppi.igpp.ucla.edu/), including the MAG (J. E. P. Connerney 2024), JADE (F. Allegrini et al. 2024), and WAVES (W. S. Kurth and C. W. Piker, 2024) dataset.

ZY acknowledges the General Program of the National Natural Science Foundation of China (grant 42374212) and the Research grants Council (RGC) General Research Fund (grant No. 17309124). YX was supported by the National Natural Science Foundation of China under grant No. 42508013, by the China Postdoctoral Science Foundation under grant No. 2025M770390, and by the Postdoctoral Fellowship Program of CPSF under grant No. GZB20250099. L.C.R. was supported by STFC grant ST/Y002148/1 to Lancaster University. Project Supported by the Specialized Research Fund for the State Key Laboratory of Solar Activity and Space Weather.

Appendix A
Details in the $B_{\mathrm{lobe-like}}$ Method

In Figure 3(a), we compare the overall distribution of $B_{\mathrm{lobe-like}}$ values with the two curves representing compressed and quiet magnetospheric states as described in Y. Xu et al. (2023). These two curves can effectively classify events at 55–80 R_J into distinct categories. At other locations, however, most events cluster within the same population and cannot be separated by the two curves.

To fit the upper and lower envelopes, we first identify the boundary points showing the range of $B_{\mathrm{lobe-like}}$ variations at different radial distances. The data points are divided into 40 equally spaced bins, from which we select the largest and the smallest $B_{\mathrm{lobe-like}}$ values in each bin, as plotted in Figure 3(b).

Adopting the functional form, $B_{\mathrm{lobe-like}} = \sqrt{\vec{B}^2_{\mathrm{dipole}} + \vec{B}^2_{\mathrm{sheet}}} = \sqrt{\frac{a}{r^6} + \frac{b}{r^n}} + c$, we tested integer n values ranging from 1 to 6 to fit other parameters using the boundary points. Both envelopes achieved optimal fitting performance at $n = 3$. Through nonlinear least-squares fitting, we obtained the following results:

$$\text{Upper Curve:} \quad B_{\mathrm{lobe-like}} = \sqrt{\frac{1.167 \times 10^8}{r^6} + \frac{4.102 \times 10^7}{r^3}} + 1.408, \quad R^2 = 0.993 \tag{A1}$$

$$\text{Lower Curve:} \quad B_{\mathrm{lobe-like}} = \sqrt{\frac{1.108 \times 10^8}{r^6} + \frac{2.454 \times 10^7}{r^3}} - 2.432, \quad R^2 = 0.995 \tag{A2}$$

The two fitted envelope curves and their performances are displayed in Figure 3(b).

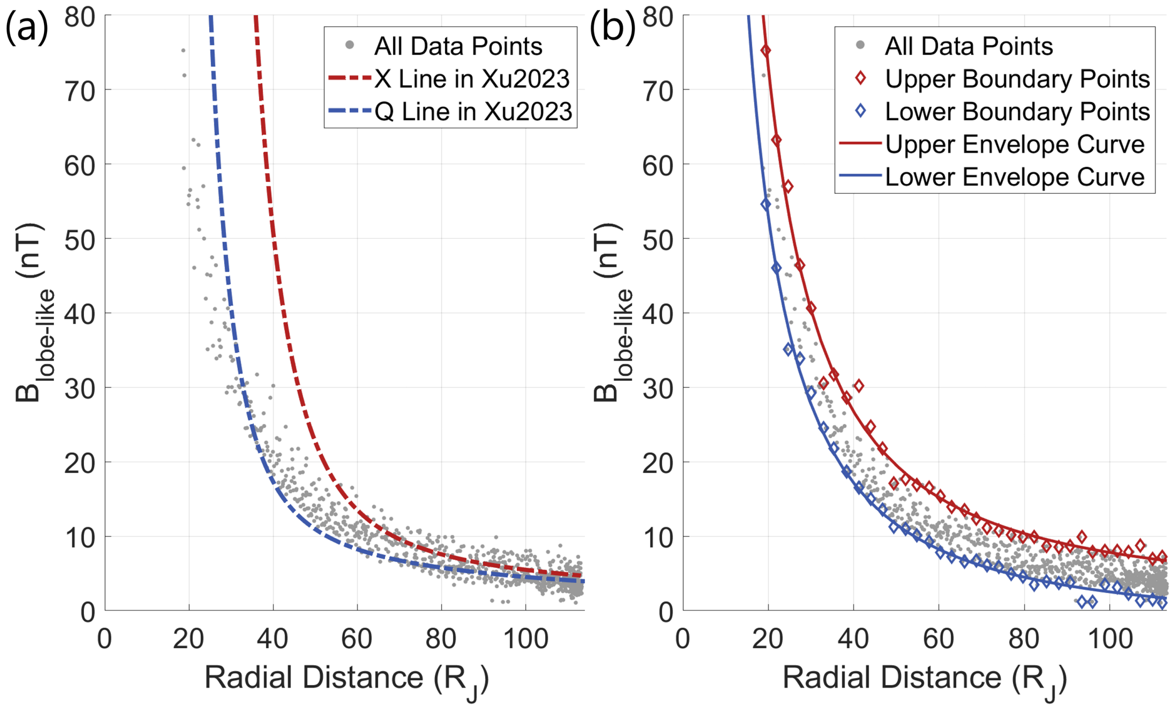

Figure 3. Distribution of $B_{\text{lobe-like}}$ values across radial distances with trend-describing curves. (a) Gray points represent $B_{\text{lobe-like}}$ values versus radial distance measured by Juno from 2016 July to 2023 July, identical to the gray points in (b). The two lines are curves provided by Y. Xu et al. (2023) describing $B_{\text{lobe-like}}$ variations under different states. During quiet auroras, $B_{\text{lobe-like}}$ values at different radial distances follow the Q line, distinct from those observed during X-family auroras (following the X line). (b) Red diamonds mark the upper boundary points of $B_{\text{lobe-like}}$ distribution, while blue diamonds indicate the lower boundary points. The red line represents the upper envelope curve fitted using upper boundary points, and the blue line shows the lower envelope derived from lower boundary points.

Appendix B
Details in the ULF Wave Method

The magnetic field-aligned (MFA) coordinate system employed in this work follows the definition: $\boldsymbol{z} = \boldsymbol{b}$ (unit vector of the background magnetic field, computed via sliding averaging), $\boldsymbol{y} = \boldsymbol{z} \times \boldsymbol{r}$ (where $\vec{r}$ is the spacecraft position unit vector), and $\boldsymbol{x} = \boldsymbol{y} \times \boldsymbol{z}$. Wavelet analysis was applied to both the total magnetic field strengths and the background-subtracted magnetic field components in the MFA coordinate system to characterize ULF wave activities in Jupiter's magnetosphere, including compressional waves, transverse waves, and overall wave activities.

To compare the responses of magnetic field fluctuations across different components to external compression, we present the magnetospheric state determination results based on wave intensities of different modes during Q/X-family aurora events in Tables 3 and 4. The diagnostic reliability increases with higher consistency between the classification results and those obtained from auroral morphology analysis. This cross-validation approach aligns with the methodology described in Section 3. Based on the comparisons, we find that using the component parallel to the background magnetic field direction for wave analysis provides the most effective identification of magnetospheric states here.

Table 3
Determination of Magnetospheric States during Q-family Aurora Intervals Based on Wave Analysis Using Different Magnetic Field Components

Index	Q-family Aurora Time (UT)	$B_{\parallel}(B_z)$	$B_{\perp 1}(B_x)$	$B_{\perp 2}(B_y)$	B_{total}
1	2016 Dec 4 12:44:51	✓	✓	✓	×
2	2016 Dec 12 14:40:35	/	/	/	/
3	2016 Dec 12 16:15:22	/	/	/	/
4	2016 Dec 13 11:21:37	/	/	/	/
5	2016 Dec 15 07:50:44	/	/	/	/
6	2017 May 10 05:54:33	✓	✓	✓	✓
7	2017 May 10 10:40:39	✓	✓	✓	✓
8	2017 May 13 08:36:44	✓	✓	✓	✓
9	2017 May 15 11:28:13	✓	✓	✓	×
10	2017 Jul 5 08:05:37	✓	✓	✓	✓
11	2017 Jul 6 23:49:38	✓	✓	✓	×
12	2017 Jul 8 04:28:27	✓	✓	✓	✓
13	2017 Jul 8 06:01:24	✓	✓	✓	✓
14	2019 Mar 9 11:10:16	/	/	/	/
15	2019 Mar 28 20:50:57	/	/	/	/
16	2019 Apr 6 14:36:00	/	/	/	/
17	2019 Sep 7 09:48:50	/	/	/	/
18	2019 Sep 10 07:42:46	×	×	×	×
19	2019 Sep 13 13:33:29	/	/	/	/

Note. The time list source and symbol definitions follow Table 1. Here, the target state refers to the quiet state.

Table 4
Determination of Magnetospheric States during X-family Aurora Intervals Based on Wave Analysis Using Different Magnetic Field Components

Index	X-family Aurora Time (UT)	$B_{\parallel}(B_z)$	$B_{\perp 1}(B_x)$	$B_{\perp 2}(B_y)$	B_{total}
1	2016 Nov 30 14:57:23	✓	×	×	×
2	2016 Nov 30 16:32:45	✓	×	×	×
3	2016 Dec 1 16:23:32	✓	✓	✓	✓
4	2016 Dec 5 18:56:58	✓	✓	✓	✓
5	2016 Dec 6 14:02:21	✓	✓	✓	✓
6	2016 Dec 11 18:29:20	/	/	/	/
7	2017 Mar 17 08:01:34	✓	✓	✓	✓
8	2017 Mar 18 14:14:38	×	×	×	✓
9	2017 Mar 19 09:19:18	✓	✓	✓	✓
10	2017 Jun 18 09:13:00	/	/	/	/
11	2019 May 22 21:24:30	✓	×	✓	×
12	2019 May 23 16:28:33	×	×	×	×
13	2019 Jul 20 13:15:38	/	/	/	/
14	2019 Sep 10 04:32:07	✓	✓	✓	×

Note. The time list source and symbol definitions follow Table 1. Here, the target state refers to the compressed state.

Appendix C
Details in the bKOM Emissions Method

Figure 4 shows Juno's trajectory in the *XY* and *YZ* planes of the JSO coordinate system during its prime mission phase from 2016 July to 2021 August. In the JSO system, the *X*-axis points from Jupiter toward the Sun, the *Z*-axis is directed northward, normal to Jupiter's orbital plane around the Sun, and the *Y*-axis completes a right-handed Cartesian triad. Juno is a polar orbiter around Jupiter, with its orbital plane precessing gradually from the dawn sector through the nightside toward the dusk sector, accompanied by an increasing orbital inclination. White dots display Juno's locations of events where the magnetospheric states determined from auroral and bKOM observations are consistent (listed in Tables 1 and 2), whereas purple dots denote events where the two methods yield different results. Event #18 in Table 1 is marked in light green; for this event, none of the three in situ methods produced a result consistent with the auroral classification. This discrepancy likely arises from factors other than the limitations of the bKOM method and is therefore not discussed further here. It can be seen that the misclassified events in Tables 1 and 2, corresponding to both quiet and compressed states, are mainly concentrated along Juno's early orbits, i.e., at large radial distances on the dawnside of Jupiter.

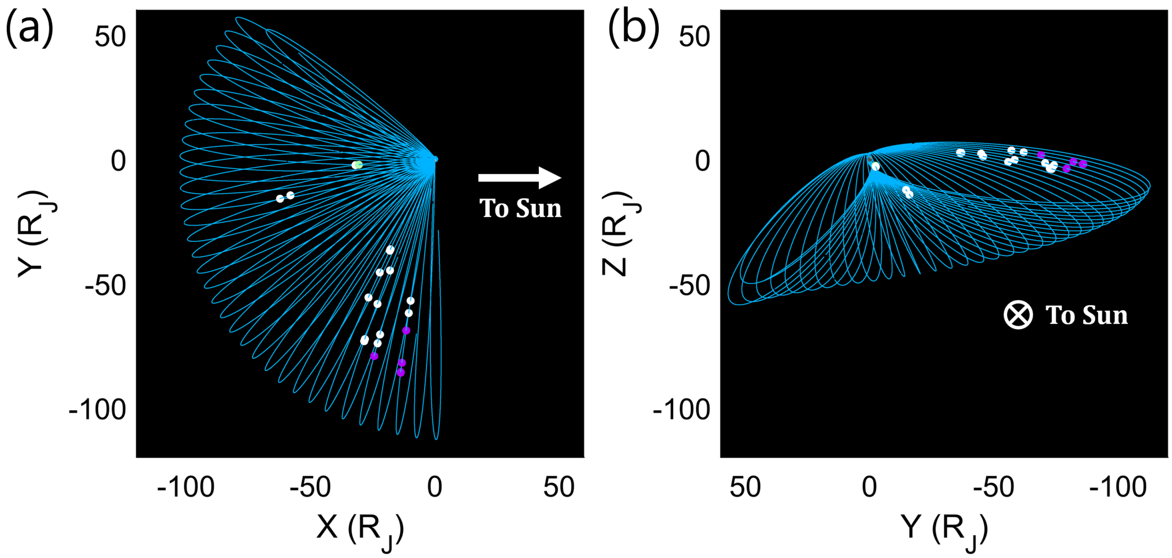

Figure 4. Juno's trajectory in the (a) *XY* and (b) YZ planes of the JSO coordinate system, where *X* points from Jupiter toward the Sun and *Z* is northward normal to Jupiter's orbital plane. White dots mark Juno's positions of events with consistent magnetospheric state identifications between auroral and bKOM methods, purple dots indicate inconsistent cases, and event #18 in Table 1 (light green) is excluded from discussion.

ORCID iDs

J. W. Sun https://orcid.org/0009-0009-2905-4372
L. Xie https://orcid.org/0000-0003-0783-932X
Z. H. Yao https://orcid.org/0000-0001-6826-2486
S. Y. Fu https://orcid.org/0000-0002-3858-1555
B. Zhang https://orcid.org/0000-0002-1555-6023
Y. Xu https://orcid.org/0000-0002-2542-9001
F. Leppard https://orcid.org/0009-0003-7928-9934
Y. N. Chen https://orcid.org/0000-0002-7079-8623
D. Grodent https://orcid.org/0000-0002-9938-4707
L. C. Ray https://orcid.org/0000-0003-3727-602X
B. Bonfond https://orcid.org/0000-0002-2514-0187
W. R. Dunn https://orcid.org/0000-0002-0383-6917

References

Allegrini, F., Wilson, R. J., Ebert, R. W., & Loeffler, C. 2024, JUNO J/SW JOVIAN AURORAL DISTRIBUTION CALIBRATED, v1.0, NASA Planetary Data System, doi:10.17189/1519715
Bagenal, F. 2007, JASTP, 69, 387
Bame, S. J., Barraclough, B. L., Feldman, W. C., et al. 1992, Sci., 257, 1539
Barnard, L., & Owens, M. 2022, FrP, 10, 1005621
Bentley, S. N., Watt, C. E. J., Owens, M. J., & Rae, I. J. 2018, JGRA, 123, 2745-2771
Bonfond, B., Yao, Z. H., Gladstone, G. R., et al. 2021, AGUA, 2, e00275
Boudouma, A., Zarka, P., Magalhães, F. P., et al. 2023, in Planetary, Solar and Heliospheric Radio Emissions IX, ed. C. K. Louis, C. M. Jackman, G. Fischer et al. (Trinity College Dublin), 103094
Bridge, H. S., Belcher, J. W., Lazarus, A. J., et al. 1979a, Sci., 204, 987
Bridge, H. S., Belcher, J. W., Lazarus, A. J., et al. 1979b, Sci., 206, 972
Cecconi, B., Witasse, O., Jackman, C. M., Sánchez-Cano, B., & Mays, M. L. 2022, FrASS, 9, 800279
Chen, Y., Ye, S., Yao, Z., & Zhang, B. 2024, ApJ, 972 (2) 154
Connerney, J. E. P. 2024, Juno MAG CALIBRATED DATA J. v1.0, NASA Planetary Data System, doi:10.17189/1519711
Connerney, J. E. P., Benn, M., Bjarno, J. B., et al. 2017, SSRv, 213, 39
Ebert, R. W., Bagenal, F., McComas, D. J., & Fowler, C. M. 2014, FrASS, 1, 4
Fischer, G., Taubenschuss, U., Píša, D., Imai, M., & Kurth, W. S. 2025, JGRA, 130, 2024JA032826
Fogg, A. R., Jackman, C. M., Waters, J. E., et al. 2022, JGRA, 127, e30209
Grodent, D., Bonfond, B., Yao, Z., et al. 2018, JGRA, 123, 3299
Groulard, A., Bonfond, B., Grodent, D., et al. 2024, Icar, 413, 116005
Gurnett, D. A., Kurth, W. S., Hospodarsky, G. B., et al. 2002, Natur, 415, 985
Head, L. A., Grodent, D., Bonfond, B., et al. 2024, A&A, 688, A205
Head, L. A., Grodent, D., Bonfond, B., et al. 2025, A&A, 700, A142
Jian, L. K., MacNeice, P. J., Taktakishvili, A., et al. 2015, SpWea, 13, 316
Keebler, T. B., Tóth, G., Zieger, B., & Opher, M. 2022, ApJS, 260, 43
Krupp, N., Woch, J., Lagg, A., et al. 2002, GeoRL, 29, 1736
Krupp, N., Woch, J., Lagg, A., et al. 2004, JGRA, 109, A09S10
Kurth, W. S., Gurnett, D. A., Hospodarsky, G. B., et al. 2002, Natur, 415, 991
Kurth, W. S., Hospodarsky, G. B., Kirchner, D. L., et al. 2017, SSRv, 213, 347
Kurth, W. S., & Piker, C. W. 2024, JUNO E/J/S/SS WAVES CALIBRATED SURVEY FULL RESOLUTION, v2.0, NASA Planetary Data System, doi:10.17189/1520498
Lamy, L., Cecconi, B., Prangé, R., et al. 2009, JGRA, 114, 10212
Louis, C. K., Jackman, C. M., Hospodarsky, G., et al. 2023, JGRA, 128, e2022JA031155
Louis, C. K., Zarka, P., Dabidin, K., et al. 2021, JGRA, 126, e29435
Manners, H., & Masters, A. 2020, JGRA, 125, e28345
McComas, D. J., Szalay, J. R., Allegrini, F., et al. 2017, GeoRL, 44, 4432
Menietti, J. D., Gurnett, D. A., Kurth, W. S., & Groene, J. B. 1999, GeoRL, 26, 569
Nichols, J. D., Badman, S. V., Bagenal, F., et al. 2017, GeoRL, 44, 7643
Nichols, J. D., Bunce, E. J., Clarke, J. T., et al. 2007, JGRA, 112, A02203
Odstrcil, D. 2003, AdSpR, 32, 497
Owens, M., Lang, M., Barnard, L., et al. 2020, SoPh, 295, 43
Palmaerts, B., Grodent, D., Bonfond, B., et al. 2024, Icar, 408, 115815
Pan, D., Yao, Z., Manners, H., et al. 2021, GeoRL, 48, e91579
Reiss, M. A., Muglach, K., Mullinix, R., et al. 2023, AdSpR, 72, 5275
Russell, C. T. 2001, P&SS, 49, 1005
Rutala, M. J., Jackman, C. M., Owens, M. J., et al. 2024, JGRA, 129, e2024JA032613
Smith, E. J., Fillius, R. W., & Wolfe, J. H. 1978, JGRA, 83, 4733
Sun, J., Xie, L., Yao, Z., et al. 2025, The event list for "Determining the State of Jupiter's Magnetosphere Using In Situ and Remote Sensing Observations", v1, Zenodo, doi:10.5281/zenodo.16355250
Sun, J. W., Xie, L., Yao, Z. H., et al. 2024, JGRE, 129, e2023JE008279
Tao, C., Kataoka, R., Fukunishi, H., Takahashi, Y., & Yokoyama, T. 2005, JGRA, 110, A11208
Xu, Y., Yao, Z. H., Zhang, B., et al. 2023, GeoRL, 50, e2023GL104123
Yao, Z., Dunn, W. R., Woodfield, E. E., et al. 2021, SciA, 7, eabf0851
Yao, Z. H., Bonfond, B., Grodent, D., et al. 2022, JGRA, 127, e2021JA029894
Yao, Z. H., Grodent, D., Kurth, W. S., et al. 2019, GeoRL, 46, 11632
Zarka, P., Magalhães, F. P., Marques, M. S., et al. 2021, JGRA, 126, e29780
Zieger, B., & Hansen, K. C. 2008, JGRA, 113, A08107
Zong, Q., Rankin, R., & Zhou, X. 2017, RvMPP, 1, 10